Hyperfine interaction of individual atoms on a surface

Authors: Philip Willke[1,2,3], Yujeong Bae[1,2,3], Kai Yang[1], Jose L. Lado[4,5], Alejandro Ferrón[6], Taeyoung Choi[2,3], Arzhang Ardavan[7], Joaquín Fernández-Rossier[4,†], Andreas J. Heinrich[2,3,*] and Christopher P. Lutz[1,*]

Affiliations:

[1] IBM Almaden Research Center, San Jose, CA 95120, USA

[2] Center for Quantum Nanoscience, Institute for Basic Science (IBS), Seoul 03760, Republic of Korea

[3] Department of Physics, Ewha Womans University, Seoul 03760, Republic of Korea

[4] QuantaLab, International Iberian Nanotechnology Laboratory (INL), Avenida Mestre José Veiga, 4715-310 Braga, Portugal

[5] Institute for Theoretical Physics, ETH Zurich, 8093 Zurich, Switzerland

[6] Instituto de Modelado e Innovación Tecnológica (CONICET-UNNE), and Facultad de Ciencias Exactas, Naturales y Agrimensura, Universidad Nacional del Nordeste, Avenida Libertad 5400, W3404AAS Corrientes, Argentina

[7] Clarendon Laboratory, Department of Physics, University of Oxford, Oxford OX1 3PU, UK.

[†] On leave from Departamento de Física Aplicada, Universidad de Alicante, San Vicente del Raspeig 03690, Spain

* E-Mail: cplutz@us.ibm.com, heinrich.andreas@qns.science

Abstract: Taking advantage of nuclear spins for electronic structure analysis, magnetic resonance imaging and quantum devices hinges on the knowledge and control of the surrounding atomic-scale environment. We measured and manipulated the hyperfine interaction of individual iron and titanium atoms placed on a magnesium oxide surface by using spin-polarized scanning tunneling microscopy in combination with single-atom electron spin resonance. Using atom manipulation to move single atoms, we found that the hyperfine interaction strongly depended on the binding configuration of the atom. We could extract atom- and position-dependent information about the electronic ground state, the state mixing with neighboring atoms, as well as properties of the nuclear spin. Thus, the hyperfine spectrum becomes a powerful probe of the chemical environment of individual atoms and nanostructures.

One Sentence Summary: Scanning tunneling microscopy gives access to individual nuclear spins by sensing and manipulating the hyperfine interaction of atoms on surfaces.

Main Text: The hyperfine interaction between an electron and a nuclear spin provides insight into the electronic structure and chemical bonding of atoms, molecules, and solids. It is also key to realizing quantum operations of the nuclear spin (*1-3*). Although most experiments rely on ensemble measurement, detection and control of single nuclear spins is possible for diluted molecules in crystals (*4*), molecules in break junctions (*3,5*), ion traps (*2*) and defects in solids (*6, 7*). Nevertheless, up to now, no experimental tool allows imaging of the atomic-scale environment of the nucleus and simultaneously resolving the hyperfine spectrum, which crucially depends on the local electronic structure.

Atomic resolution along with atom manipulation has been achieved by scanning probe methods, and they have been used to study the local electronic structure of atoms and molecules. Scanning probes allow chemical identification (*8*) and imaging of chemical bonds (*9*) and they provide access to the structure (*10*) and dynamics (*11*,*12*) of electron spins. The nuclear properties detected in scanning tunneling microscopy (STM) include changes in vibrational (*13*) and rotational (*14*) motion, but the hyperfine interaction has not previously been resolved due to a limited resolution in energy (*15*,*16*).

Combining STM with electron spin resonance (ESR) as demonstrated for individual iron (Fe) (*17*,*18*) and titanium (Ti) atoms (*19*,*20*) potentially provides the required energy resolution. However, no hyperfine splitting was reported so far. For atoms having low natural abundances of magnetic nuclei (such as Fe) or multiple magnetic isotopes (such as Ti) it is necessary to study a large number of individual atoms to establish the hyperfine physics. Here we present such a study, aided by new understanding of the tunneling parameters (*21*) that improves the signal-to-noise ratio compared to previous ESR-STM experiments (*17*,*18*).

Individual Fe and Ti atoms from sources having natural isotopic abundance were deposited on two atomic layers of MgO grown on silver (*22*). First, we examined Fe atoms adsorbed onto an oxygen binding site of the MgO (*23*) (Fig. 1A). We resonantly excited transitions between the electronic ground state (spin-up) and the first excited state (spin-down) of the Fe atom by using ESR. We used a magnetic field $B = 0.9$ T and a temperature of $T = 1.2$ K unless stated otherwise. This excitation led to a change in tunnel current ΔI when driven at the resonance frequency (*17*) (Fig. 1B). A magnetic tip was used for magnetoresistive readout leading to different conductance for the two electronic states.

For 3.4% of Fe atoms (5 out of 147, see inset in Fig. 1B) investigated the ESR peak was split by $\Delta f = 231 \pm 5$ MHz, which we attributed to the presence of a nuclear moment $I = 1/2$ for ^{57}Fe (2.1% natural abundance). In contrast, the $I = 0$ isotopes, predominantly ^{56}Fe, showed no splitting. We could not distinguish different $I = 0$ isotopes and label them ^{56}Fe for simplicity. Because the hyperfine splitting Δf is much smaller than the thermal energy $k_B T \approx 25$ GHz, the two nuclear states $m_I = \pm 1/2$ are occupied with equal probability. Thus, the ^{57}Fe peaks each had half the ESR peak height of the single peak observed for ^{56}Fe. Moreover, the simultaneous presence of two peaks indicates that the nuclear spin relaxation time was here much shorter than the time scale of the measurement (~1 ms) (*22*).

For the magnetic field used here, the electronic Zeeman energy is large compared to the hyperfine interaction. Because the Fe atom on MgO shows a large out-of-plane magnetic anisotropy, the electron spin is quantized along the out-of-plane direction z (*23*). Thus, the nuclear spin was quantized along z as well, leading to the spin Hamiltonian (*24*)

$$H = g_z \mu_B B_z S_z + A_z I_z S_z \quad (1)$$

where μ_B is the Bohr magneton and S_z and I_z are the z-axis spin operators for the electron and nuclear spin, respectively. Parameters g_z and A_z are the z components of the electron g-factor and the hyperfine coupling constant, respectively. B_z is the z component of the magnetic field. The very small nuclear Zeeman energy is neglected here.

Determining the eigenstates of Eq. (1), the spins can either be aligned or anti-aligned with the magnetic field, to give product states $|m_S, m_I\rangle$ where m_S and m_I are the electron and nuclear quantum numbers (Fig. 1C). Transitions occurred between the $m_S = \pm 2$ electronic states ($\Delta m_S =$

4) (*17*) and left the nuclear spin state unchanged ($\Delta m_I = 0$), leading to one resonance peak for ^{56}Fe. The spectra were centered at frequency f_0 given by the Zeeman energy $hf_0 = g_z \mu_B B_z \Delta m_S$. The two frequencies observed for ^{57}Fe in Fig. 1B differed because of the relative alignment of the electron and nuclear spin, to give a peak splitting $\Delta f = \Delta m_S \Delta m_I A_z = 4A_z$ where $\Delta m_I = 1$ (*24*).

In contrast to Fe, the hyperfine interaction of Ti atoms was more complex and reflected changes in the local electronic environment (*24*). The Ti atoms studied here were hydrogenated (*19*), resulting in an electronic spin-1/2 that lacked magnetic anisotropy. Thus, to good approximation, the electron spin followed the magnetic-field direction (*19*,*20*). The hyperfine spectra for Ti located on a bridge binding site (Ti_B) of MgO (*20*) (Fig. 2) showed $2I + 1$ peaks, one for each nuclear spin state, resulting in six peaks for ^{47}Ti ($I = 5/2$, 7.4% natural abundance), eight peaks for ^{49}Ti ($I = 7/2$, 5.4%), and a single peak for the nuclear spin free isotopes, predominantly ^{48}Ti ($I = 0$, 73.7%). We found a splitting Δf between adjacent peaks of ~47 MHz for both ^{47}Ti and ^{49}Ti, implying that their nuclear gyromagnetic ratios were equal [See section 2 in (*22*)]. For all investigated atoms, we found no appreciable dependence of the hyperfine splitting on the magnetic field caused by the proximity of the tip (*19*), nor on the local electric field induced by the DC bias voltage.

In contrast to ensemble measurements, the binding site of individual atoms could be determined from STM images, and the atom could be moved among binding sites by using atom manipulation. We moved a ^{47}Ti atom to different binding sites (Fig. 3A). We observed a drastic reduction of the splitting Δf to ~10 MHz (Fig. 3B) when the Ti atom was moved from a bridge to an oxygen site (Ti_O). The larger splitting was restored by moving the same atom back to a bridge binding site. In Fig. 3C we show the exact position of the atoms obtained from Fig. 3A and show density functional theory (DFT) calculations (*22*) of the respective electronic ground state. The statistics for different atoms on the same type of binding site (Fig. 3D) revealed a small but reproducible difference in Δf for the two inequivalent bridge binding sites. This difference was caused by different values of $g_x \neq g_y$ and $A_x \neq A_y$ (resulting from the low symmetry of the bridge binding site) along with a magnetic field direction $B_x \neq B_y$ [Fig. 3C and section 1 in (*22*)].

Hyperfine spectra for both isotopes of Ti_O are shown in high resolution in Fig 3E. In addition to the strong decrease in Δf compared to Ti_B, the interval between peaks as well as their amplitudes were non-uniform. To describe the spectra, we generalize the hyperfine Hamiltonian in Eq. (1) to

$$H = H_{\mathrm{EZ}} + H_{\mathrm{HF}} + H_{\mathrm{NQ}} \tag{2}$$

Here, $H_{\mathrm{EZ}} = \mu_B \sum_{i=x,y,z} g_i B_i S_i$ and $H_{\mathrm{HF}} = \sum_{i=x,y,z} A_i I_i S_i$ were generalized to include the x and y spin components, needed for electronic spins lacking strong anisotropy (*19*), and the hyperfine interaction was allowed to have anisotropy. Moreover, $H_{\mathrm{NQ}} = \sum_{i=x,y,z} P_i I_i^2$ is the nuclear electric quadrupole interaction, caused by the electric field gradient at the position of the nucleus (*24*). This quadrupole term is irrelevant for $I = 1/2$ systems, as in the case of Fe (*24*). Using the known symmetry of the system, only three fit parameters, A_z, $A_x = A_y$ and P_z were required to give good fits to the complex hyperfine spectrum of Ti_O (*22*). Simulated ESR spectra of the experimental data using EasySpin (*25*) are superimposed on the data in Fig. 3E. The fits reflect that the hyperfine and the nuclear quadrupole interaction have comparable energies for Ti_O, resulting in peaks that are irregularly spaced because they are not well approximated by eigenstates of either operator alone. Furthermore, these measurements allowed us to determine the ratio of the nuclear quadrupole moments of $^{49}Q/^{47}Q \approx 0.79$. The excellent agreement with ensemble measurements

[$^{49}Q/^{47}Q = 0.82$ (*26*)] shows the fidelity of the model and that good accuracy was obtained with this limited number of fit parameters.

Although the electric quadrupole interaction changed the peak intensities and spacings for Ti_O, the overall reduction in Δf compared to Ti_B was caused by the reduction in the hyperfine coupling constant $\boldsymbol{A}$. We consider here two contributions (*24*). The first is the isotropic Fermi contact term originating from a finite spin-density of unpaired s-electrons at the nucleus induced by interaction with the d-electrons. The second is the anisotropic magnetic dipolar interaction of the nuclear spin with the surrounding d-electrons and depends on the orbital symmetry (*27*). The observed changes in Δf for the different binding sites of Ti were caused by the occupation of different orbitals in the magnetic ground state of the atom (Fig. 3C). We found a larger Fermi contact contribution for Ti_B ($+50$ MHz) compared to Ti_O ($+19$ MHz), presumably caused by a difference in covalency (*24*) [Section 2 in (*22*)].

More importantly, the three spatial components of the dipolar contribution changed in magnitude and sign for the different binding sites. Because the magnetic field was applied nearly in-plane (Fig. 1A), the in-plane components A_x and A_y contributed the most to Δf. In case of Ti_B, the dipolar contribution added to the Fermi contact part for one of the two components ($A_x \approx +61$ MHz; $A_y \approx +29$ MHz). In contrast, for Ti_O, both in-plane directions opposed the Fermi contact interaction resulting in $A_x = A_y \approx +10$ MHz. As a result, Δf is smaller for Ti_O than Ti_B. The strength of the hyperfine interaction and the importance of quadrupole interaction revealed the profound change in the chemical environment of the Ti atom upon moving it from a bridge site to an oxygen site: Modelling the hyperfine interaction and taking the DFT ground state into account we find that the bonding with oxygen reduces the electron spin density at the Ti nucleus for Ti_O [~ -1 a. u. instead of ~ -2.8 a. u. for Ti_B (*22*)]. Moreover, the radial spread of the spin-polarized orbital $\langle r^{-3} \rangle$ can be deduced from the hyperfine splitting and the electric quadrupole contribution, which lies for both binding sites at $\sim(0.5\ \text{Å})^{-3}$(*22*).

Hyperfine spectra can also reveal changes in the magnetic environment, as we demonstrate here using assembled structures of Ti atoms. Figure 4A shows a $^{47}Ti_B$ atom with a nuclear spin $I = 5/2$ that was moved to a position $\sim$7 Å from a $^{48}Ti_O$ atom ($I = 0$). Because of the exchange interaction between the electronic spins, an electronic singlet-triplet system was formed [Fig. 4B, right, and section 3 in (*22*)] (*19,20*). The Zeeman term split the triplet states (T_-, T_0, T_+), whereas the energies of both the singlet S_0 and the triplet state T_0 remained independent of magnetic field.

Analogously, the hyperfine interaction did not split either S_0 or T_0 and for the T_+ and T_- states, the splitting remained the same as for the single atom (Fig. 4B). Thus, the hyperfine splitting for the T_-T_0 transition, which involved one of the magnetic-field-independent states (T_0), decreased to only 27.2 ± 0.4 MHz, roughly half the value of the isolated Ti case (Fig. 4C). Accordingly, the hyperfine splitting of the singlet-triplet transition (S_0T_0) in Fig. 4C was essentially zero (less than our $\sim$10 MHz linewidth). These transitions allowed us to probe the polarization of the coupled-atom states and to quantify the degree of state-mixing to 87% in the singlet state [section 3 in (*22*)]. Note that here $\boldsymbol{A}$ remained constant and instead the electronic spin magnetization was changed (*20*). This Ti dimer structure showed that the collective properties that emerged in a correlated multispin structure yielded characteristics sharply different than those of the constituents.

References and Notes:

1. B. E. Kane, *Nature* **393**, 133–137 (1998).
2. B. B. Blinov, D. Leibfried, C. Monroe, D. J. Wineland, *Quantum Information Processing* **3**, 45–59 (2004).
3. S. Thiele *et al.*, *Science* **344**, 1135–1138 (2014).
4. J. Köhler, A. C. J. Brouwer, E. J. J. Groenen, J. Schmidt, *Science* **268**, 1457–1460 (1995).
5. R. Vincent, S. Klyatskaya, M. Ruben, W. Wernsdorfer, F. Balestro, *Nature* **488**, 357–360, (2012).
6. P. Neumann *et al.*, *Science* **329**, 542–544 (2010).
7. J. J. Pla et al., *Nature* **496**, 334–338 (2013).
8. Y. Sugimoto *et al.*, *Nature* **446**, 64–67 (2007).
9. L. Gross, F. Mohn, N. Moll, P. Liljeroth, G. Meyer, *Science* **325**, 1110–1114 (2009).
10. A. J. Heinrich, J. A. Gupta, C. P. Lutz, D. M. Eigler, *Science* **306**, 466–469 (2004).
11. S. Loth, M. Etzkorn, C. P. Lutz, D. M. Eigler, A. J. Heinrich, *Science* **329**, 1628–1630 (2010).
12. A. A. Khajetoorians *et al., Science* **339**, 55–59 (2013).
13. B. C. Stipe, M. A. Rezaei, W. Ho, *Science* **280**, 1732–1735 (1998).
14. F. D. Natterer, F. Patthey, H. Brune, *Phys. Rev. Lett.* **111**, 175303 (2013).
15. F. Delgado, J. Fernández-Rossier, *Phys. Rev. Lett.* **107**, 076804 (2011).
16. C. R. Ast *et al.*, *Nat. Commun.* **7**, 13009 (2016).
17. S. Baumann *et al*., *Science* **350**, 417–420 (2015).
18. W. Paul, S. Baumann, C. P. Lutz, A. J. Heinrich, *Rev. Sci. Instrum.* **87**, 074703 (2016).
19. K. Yang *et al.*, *Phys. Rev. Lett.* **119**, 227206 (2017).
20. Y. Bae *et al.*, submitted (2018).
21. P. Willke *et al.*, *Sci. Adv.* **4**, eaaq1543 (2018).
22. Materials and methods are available as supplementary materials on Science Online.
23. W. Paul *et al.*, *Nat. Phys.* **13**, 403–407 (2017).
24. A. Abragam, B. Bleaney, Electron paramagnetic resonance of transition ions (OUP Oxford, Reprinted Ed. 2012).
25. S. Stoll, A. Schweiger, *J. Magn. Res.* **178**, 42–55 (2006).
26. K. H. Channappa, J. M. Pendlebury, *Proc. Phys. Soc.* **86**, 1145–1146 (1965).
27. F. E. Mabbs, D. Collison, *Electron paramagnetic resonance of d transition metal compounds* (Vol. 16). Elsevier (2013).
28. T. Choi *et al.*, *Nat. Nanotechnol.* **12**, 420–424 (2017).

29. J. J. van der Klink, H. B. Brom, *Prog. Nucl. Magn. Reson. Spectrosc.* **36**, 89-201 (2000).

30. B. R. McGarvey, *J. Chem. Phys.* **71**, 51–66 (1967).

31. W. J. Childs, L. S. Goodman, *Phys. Rev.* **148**, 74–78 (1966).

32. T. P. P. Hall, W. Hayes, R. W. H. Stevenson, J. Wilkens, *J. Chem. Phys.* **39**, 35–39 (1963).

We thank Bruce Melior for expert technical assistance and William Paul, Fabian Natterer and Shadi Fatayer for further discussions. **Funding:** We gratefully acknowledge financial support from the Office of Naval Research. P.W., Y.J.B., T.C. and A.J.H. acknowledge support from the Institute for Basic Science under grant IBS-R027-D1. A.F. acknowledges CONICET (PIP11220150100327) and FONCyT (PICT-2012- 2866). J.L.L is grateful for financial support from ETH Fellowship program. J.F.-R. thanks the Fundação para a Ciência e a Tecnologia, under project no. PTDC/FIS-NAN/4662/2014 (016656). A.A. thanks the Engineering and Physical Sciences Research Council under project no. EP/L011972/1. P.W. acknowledges support from the Alexander von Humboldt Foundation. **Authors contributions:** A.J.H. and C.P.L. supervised the project. P.W., Y.B., K.Y. and T.C. carried out the STM measurements. P.W. performed the analysis and wrote the manuscript with help from all authors. A.F., J.L.L., and J.F-R. performed the DFT calculations. All authors discussed the results and edited the manuscript. **Competing interests:** None declared. **Data and materials availability:** All data needed to evaluate the conclusions in the paper are present in the paper and/or the Supplementary Materials. Additional data related to this paper may be requested from the authors.

Supplementary Materials:

Figures S1-S4

Tables S1

References (*28-32*)

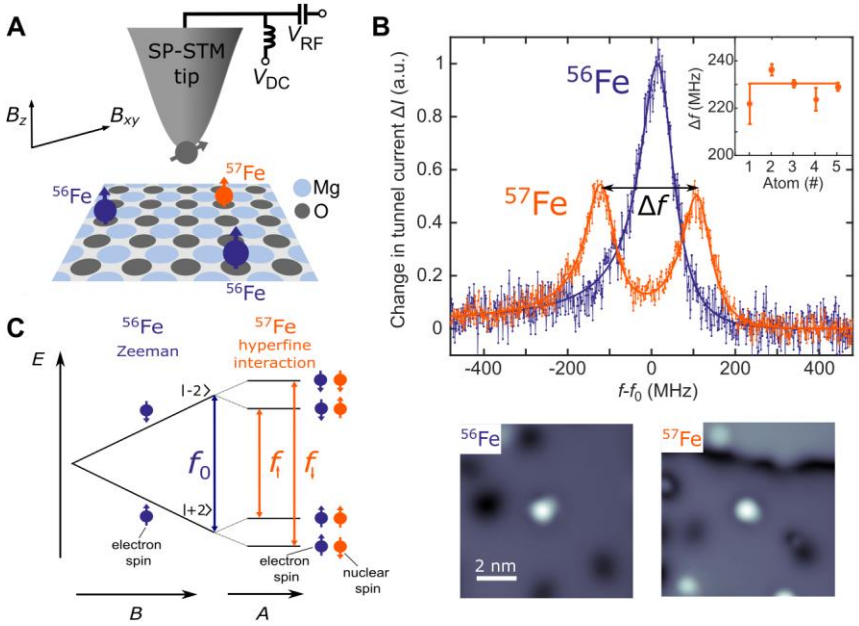

Fig. 1. **Hyperfine interaction studied by electron spin resonance (ESR) in a scanning tunneling microscope (STM). (A)** Experimental setup showing different isotopes of single Fe atoms on a bilayer MgO film on Ag(001) in an STM ($B = 0.9$ T, $B_z = 0.1$ T, $T = 1.2$ K). ESR was performed by applying a radio frequency (RF) voltage V_{RF} to the tunneling junction (*17*,*18*). **(B)** ESR spectra of the change in tunnel current for different Fe isotopes. Blue: Fe having zero nuclear spin (likely ^{56}Fe; see main text). Orange: ^{57}Fe with nuclear spin $I = 1/2$. Spectra were normalized to unity for ^{56}Fe. Electron Zeeman energy gives the center frequency f_0, here 19.89 GHz for ^{56}Fe and 19.87 GHz for ^{57}Fe (tunnel conditions: $I_{\mathrm{set}} = 12$ pA, $V_{\mathrm{DC}} = 60$ mV, $V_{\mathrm{RF}} = 60$ mV). Inset: Peak splitting Δf for five different ^{57}Fe atoms. Solid line indicates the error-weighted mean. Lower part: Topographic images of both atoms. **(C)** Schematic of the energy levels of the ^{56}Fe atom, compared to that of ^{57}Fe including hyperfine interaction as a function of the external magnetic field B and the hyperfine constant A (the small nuclear Zeeman energy was neglected).

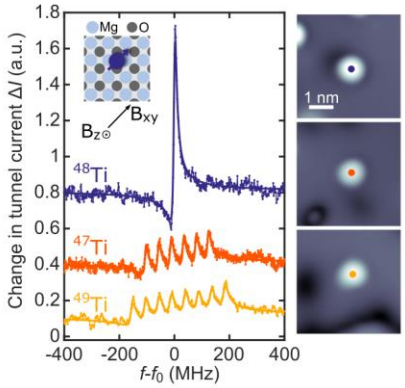

Fig. 2. Hyperfine interaction for titanium on a bridge binding site. ESR spectra for ^{48}Ti (blue, nuclear spin $I = 0$), ^{47}Ti (orange, $I = 5/2$) and ^{49}Ti (yellow, $I = 7/2$). Inset: bridge binding site. Right panel: STM images for each atom (Experimental conditions for ^{48}Ti: $f_0 = 23.03$ GHz, $I_{\mathrm{set}} = 8$ pA, $V_{\mathrm{DC}} = 40$ mV, $V_{\mathrm{RF}} = 30$ mV. For ^{47}Ti: $f_0 = 22.99$ GHz, $I_{\mathrm{set}} = 8$ pA, $V_{\mathrm{DC}} = 40$ mV, $V_{\mathrm{RF}} = 30$ mV. For ^{49}Ti: $f_0 = 22.69$ GHz, $I_{\mathrm{set}} = 20$ pA, $V_{\mathrm{DC}} = 60$ mV, $V_{\mathrm{RF}} = 40$ mV).

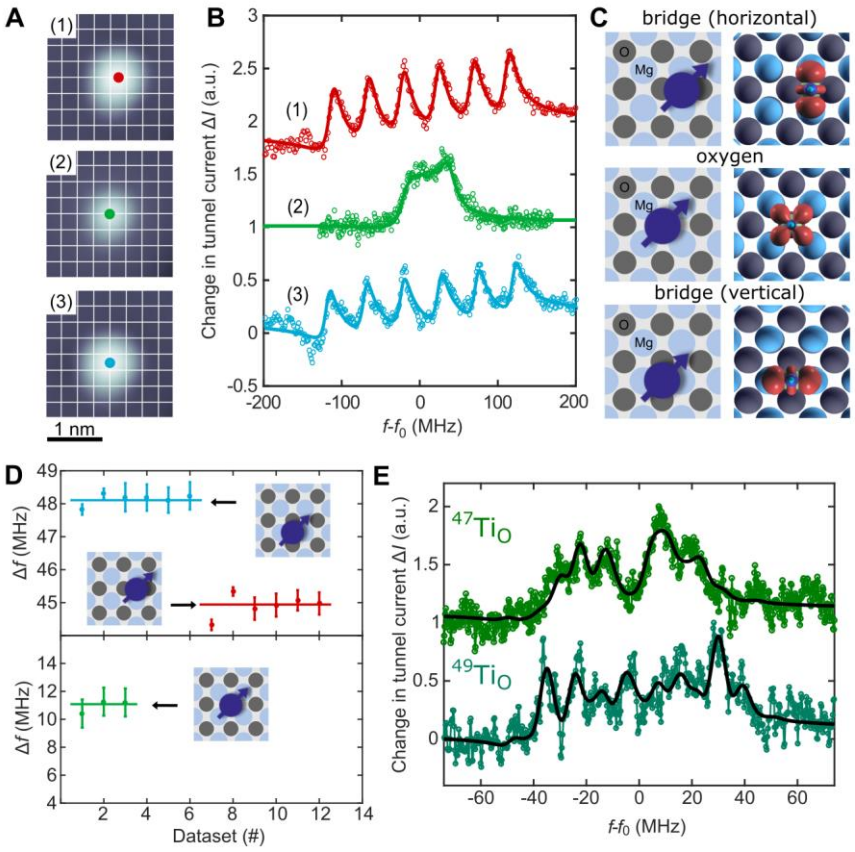

Fig. 3. Binding site dependence of the hyperfine spectrum of titanium. (A) Using atom manipulation, a ^{47}Ti atom on a bridge site (Ti_B) was moved to an oxygen binding site (Ti_O) and subsequently to a different bridge binding site. White lines indicate the MgO lattice with the intercepts corresponding to the positions of oxygen atoms. **(B)** ESR spectra for the binding sites in (A) [(1): $I_{set} = 10$ pA, $V_{DC} = 40$ mV, $V_{RF} = 40$ mV, $f_0 = 22.89$ GHz / (2): $I_{set} = 10$ pA, $V_{DC} = 60$ mV, $V_{RF} = 7$ mV, $f_0 = 22.91$ GHz / (3): $I_{set} = 10$ pA, $V_{DC} = 40$ mV, $V_{RF} = 40$ mV, $f_0 = 22.69$ GHz]. **(C)** Sketches (left) show the binding site. Calculated spin density (right) of the binding configurations obtained by DFT. **(D)** Statistics of the hyperfine splitting Δf for the different binding sites [horizontal bridge site in red: $\Delta f = 44.9 \pm 0.5$ MHz, vertical bridge site in blue: $\Delta f = 48.1 \pm 0.3$ MHz and oxygen site in green: $\Delta f = 10.8 \pm 0.7$ MHz. For the latter, Δf was obtained by neglecting electric quadrupole interaction which leads to unequal spacing of the peaks]. **(E)** High-resolution ESR spectra for ^{47}Ti (top, $I_{set} = 1.5$ pA, $V_{DC} = 60$ mV, $V_{RF} = 25$ mV, $T = 0.6$ K, $f_0 = 22.49$ GHz) and ^{49}Ti (bottom, $I_{set} = 2.5$ pA, $V_{DC} = 60$ mV, $V_{RF} = 25$ mV, $T = 0.6$ K, $f_0 = 22.49$ GHz) on oxygen binding site. Black lines are fits to the data including the anisotropic hyperfine and nuclear electric quadrupole interaction (see main text).

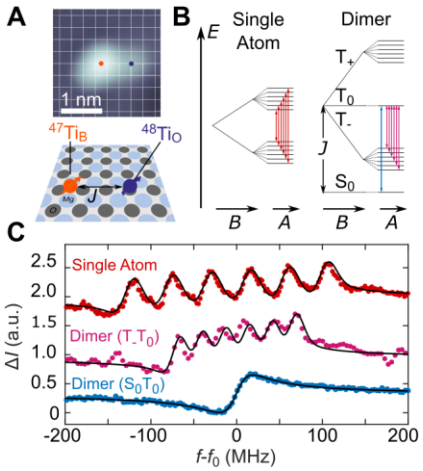

Fig. 4. Tuning the hyperfine splitting of a coupled two-atom nanostructure. (A) Topography of a dimer of Ti atoms created using atom manipulation (left: Ti_B, right: Ti_O, separation 7.2 Å). The bridge-site atom has a nuclear magnetic moment ($^{47}Ti_B$, $I = 5/2$); the oxygen-site atom is nuclear-spin-free ($^{48}Ti_O$, $I = 0$). **(B)** Energy levels of the single $^{47}Ti_B$ atom (left) and the dimer (right). For the dimer, the electronic spins form a singlet-triplet system due to exchange coupling [coupling strength $J/h = (29.1 \pm 0.2)$ GHz]. **(C)** ESR spectrum of the transitions between T_0 and T_- taken on $^{47}Ti_B$ in the dimer reveals a decrease in hyperfine splitting Δf (middle, $I_{set} = 10$ pA, $V_{DC} = 40$ mV, $V_{RF} = 20$ mV, $f_0 = 22.89$ GHz) compared to the isolated case (top, same data as Fig. 2A). In the case of the singlet-triplet transition, S_0T_0, no hyperfine splitting was observed (bottom, $I_{set} = 5$ pA, $V_{DC} = 40$ mV, $V_{RF} = 20$ mV, $f_0 = 29.72$ GHz).

Supplementary Materials for

Hyperfine Interaction of individual atoms on a surface

Philip Willke[1,2,3], Yujeong Bae[1,2,3], Kai Yang[1], Jose L. Lado[4,5], Alejandro Ferrón[6], Taeyoung Choi[2,3], Arzhang Ardavan[7], Joaquín Fernández-Rossier[4,†], Andreas J. Heinrich[2,3,*] and Christopher P. Lutz[1,*]

correspondence to: cplutz@us.ibm.com, heinrich.andreas@qns.science

This PDF file includes:

Materials and Methods

Sample Preparation

For sample preparation, the Ag(001) substrate was cleaned by several cycles of Argon-sputtering and annealing at ~750 K. For MgO growth the sample was held at ~600 K under Mg flux from a Knudsen cell and in an oxygen environment of ~$1x10^{-6}$ torr. Two monolayers of MgO were grown using a growth rate of ~0.5−1 monolayers per minute.

Fe and Ti atoms were transferred onto the sample using e-beam evaporation from metal rods having natural isotopic abundance. Evaporation was performed in-situ directly onto the cold MgO/Ag(001) sample (<10 K). The density of Fe and Ti atoms was chosen by repetitive evaporation to lie between $0.01-0.1$ atoms$/\mathrm{nm}^2$. This number was found to be appropriate to conveniently study sufficient numbers of atoms, but avoid interaction between them due to magnetic dipole or exchange coupling (*19*,*28*).

For the STM tip an iridium wire was used. The tip apex is assumed to be covered by silver due to indentations into the Ag(001) substrate in order to prepare the tip. To obtain a magnetic tip, Fe atoms were picked up from the surface (usually ~1−5 atoms) until spin contrast and ESR signal was obtained.

For atom manipulation, the tip-sample distance was decreased to a typical junction resistance of 50 MΩ ($I_{\mathrm{set}} = 7$ nA, $V_{\mathrm{DC}} = 350$ mV).

Statistics of the abundance

In total, we measured 147 Fe atoms from May 2015 to June 2018. Five of these were identified as ^{57}Fe by observing the hyperfine splitting. This corresponds to an abundance of $3.4 \pm 1.5\%$ (using sample standard error). For Ti we found 9 ^{47}Ti atoms and 2 ^{49}Ti atoms among 103 $\mathrm{Ti_B}$ atoms leading to $8.7 \pm 2.8\%$ and $1.9 \pm 1.4\%$, respectively.

These values are close to the natural abundances: 2.1%, 7.4% and 5.4% for ^{57}Fe, ^{47}Ti and ^{49}Ti, respectively. Some systematic errors may be present in our measurement of the isotopic abundances. For example, the ESR linewidth for some measurements may have been too broad to identify the hyperfine splitting of some atoms having $I \neq 0$. This likely happened in case of $\mathrm{Ti_O}$ atoms, where the hyperfine splitting is smallest, which is why we chose only $\mathrm{Ti_B}$ for the statistics of Ti above. In addition, some sampling bias may have occurred because some atoms were provisionally probed during the process of set up and calibration, and subsequently confirmed only when they appeared to be the isotope sought for the experiment at hand.

Assignment of binding sites in atom manipulation experiments

In Fig. 3 and Fig. 4 in the main text we used atom manipulation to move Ti atoms to different binding sites and to form dimers, respectively. The binding sites of $\mathrm{Ti_O}$, $\mathrm{Ti_B}$ and Fe were determined in previous experiments(*19*,*20*,*28*). The atomic species can be distinguished by the topographic height, spectroscopic measurements (dI/dV-spectroscopy) and the ESR spectra. The piezo constants were calibrated using atomically resolved STM images of the MgO lattice.

Fig. S1 depicts an STM image on a larger scale of the Ti atom shown in Fig. 3 in the main text. The positions of the surrounding atoms in all figures served as references to track the change in position [See supplementary section 1 in Ref. (*28*) for a detailed description of this method]. In this analysis, we additionally used the positions from several bridge-site lattice positions to which the central Ti atom under study was moved (see Fig S4) for the calibration of the lattice.

Fig. S2 shows the position of the dimer in Fig. 4a in the main text. Here, the lattice was calibrated at reference atoms at a different position. Again, information about the atomic species obtained from their topographic height and spectroscopic features was taken into account to identify the binding site and the relative distance between the atoms (*19,20*). Additional information about the creation of these dimers using atom manipulation can be found in Ref. (*20*).

For the main text the images were rotated by ~45° compared to Figs. S1 and S2 to align the MgO lattice in x- and y-direction.

Time scales of the experiment

We here use continuous wave (cw) ESR, which uses continuous excitation of the electron spin. The measurement time scale in our experiment was $T_{\mathrm{measure}} \approx 1$ ms. The spectra observed in the main text always showed multiple ESR peaks corresponding to all possible nuclear spin states. Moreover, no switching or additional noise in the tunnel current was observed when the frequency was held constant at a particular peak. Therefore, the time scale of nuclear spin-flips $T_{1,\,\mathrm{nuclear}}$ has to be shorter than the measurement time scale: $T_{1,\,\mathrm{nuclear}} < T_{\mathrm{measure}}$. As a result, the ESR spectra give the mean thermal population of the nuclear spin, which is almost equally distributed among all nuclear states.

The spin-lattice relaxation due to phonons can be estimated to be $\sim 0.1-10$ s using Table 5 in Ref. (*29*). These are therefore unlikely to be the dominant cause of nuclear spin relaxation. We propose that the relaxation process is driven by the hyperfine coupling between the nucleus and its own electron spin in combination with coupling to itinerant electrons that tunnel from the nearby conduction baths of tip and sample. Similarly, tunneling electrons were shown to cause spin relaxation for the electron spin of Fe atoms (*23*). This includes electrons starting and ending in the Ag(001) substrate, the tip, or that pass between electrodes in either direction. For the tunnel currents used here ($1-20$ pA) the time-scale of the tunneling electrons $T_{\mathrm{e}} = \frac{\mathrm{e}}{I} \approx 10-100$ ns. In addition, thermally excited electrons from the substrate can lead to an additional current of ~ 1 pA (*23*) at 1 K. This frequent presence of the tunneling electrons likely explains the short $T_{1,\,\mathrm{nuclear}}$.

Density functional theory

In this section we focus on the energetics of individual Ti ad-atoms. Density functional theory (DFT) calculations were performed with Quantum Espresso, using projected augmented wave pseudopotentials, PBE exchange correlation functional and 50-70 Ry of plane wave energy cut-off as described elsewhere (*19*). We performed calculations in a structure formed by a bilayer of MgO together with the hydrogenated Ti (with one H). The removal of silver from the calculations minimizes spurious effects due to the limitations of DFT to capture simultaneously metallic states and localized moments. The main distortions created by the ad-atom in the MgO bilayer are: (i) an upward displacement of the closest oxygen(s) to ad-atoms and (ii) a distortion downwards of the Mg atoms located below the Ti-bonded oxygen atoms.

We found that both for the binding site of on-top-of-oxygen ($\mathrm{Ti_O}$) and for the bridge position ($\mathrm{Ti_B}$), a hydrogenated Ti atom shows $S = 1/2$. We show in Fig. 3C in the main text the spin densities for the two conformations mentioned above, imposing C4 symmetry and C2 symmetry in the unit cell for the on-top-of-oxygen and bridge structure, respectively. The spin density of hydrogenated $\mathrm{Ti_O}$ (with the Ti and H atoms located collinear along the z axis) is consistent with a filling of the $\mathrm{d_{xy}}$ orbital. The previous results are easily rationalized by a crystal

field combination of an axial term plus a square term, yielding a d_{xy} orbital as the lowest energy level, pointing towards the Mg atoms. The ground state of Ti_B has a spin density that resembles an orbital d_{y2}, taking the y-direction as the in-plane axis perpendicular to a line that connects two oxygens. Of course, this changes to a d_{x2} orbital for the other possible bridge site position.

For the case of the hydrogenated Ti, the precise position of the H atom with respect to the Ti is expected to be influenced by the silver substrate, the STM tip and the applied voltage. We have verified that different conformations of the H atom always give spin $S = 1/2$, yielding the magnetic properties independent of the specific structural configuration.

Supplementary Text

Section 1: Fitting the hyperfine structure

Section 1.1: Fitting the hyperfine structure: The Spin Hamiltonian

In the framework of this work all necessary contributions can be summarized in the spin Hamiltonian (*24*,*25*)

$$\widehat{H} = \widehat{H}_{EZ} + \widehat{H}_{HF} + \widehat{H}_{NQ} = \mu_B \boldsymbol{B}^{\mathrm{T}} \boldsymbol{g} \widehat{\boldsymbol{S}} + \widehat{\boldsymbol{S}}^{\mathrm{T}} \boldsymbol{A} \widehat{\boldsymbol{I}} + \widehat{\boldsymbol{I}}^{\mathrm{T}} \boldsymbol{P} \widehat{\boldsymbol{I}} \tag{S1}$$

Where $\widehat{H}_{EZ}$, $\widehat{H}_{HF}$ and $\widehat{H}_{NQ}$ denote the electron Zeeman interaction, the hyperfine interaction and the nuclear quadrupole interaction, respectively. We neglect nuclear Zeeman interaction $\widehat{H}_{NZ} = \mu_N \boldsymbol{B}^{\mathrm{T}} \boldsymbol{g}_N \widehat{\boldsymbol{I}}$, since it is much smaller than all other contributions (*24*,*25*).

The hyperfine coupling tensor can be written in the diagonal form (*24*,*25*)

$$\boldsymbol{A} = A_{\mathrm{S}} \boldsymbol{I} + \boldsymbol{T} = \begin{pmatrix} A_{\mathrm{S}} & 0 & 0 \\ 0 & A_{\mathrm{S}} & 0 \\ 0 & 0 & A_{\mathrm{S}} \end{pmatrix} + T \begin{pmatrix} -(1-\rho) & 0 & 0 \\ 0 & -(1+\rho) & 0 \\ 0 & 0 & 2 \end{pmatrix} \tag{S2}$$

with the isotropic Fermi-contact interaction

$$A_{\mathrm{S}} = \left(\frac{2}{3} \frac{\mu_0}{h} g_N g_e \frac{\mu_N}{I} \mu_e \right) \chi \tag{S3}$$

where μ_0 is the vacuum permittivity. g_N and μ_N are the g-factor and magneton of the nuclear spin, respectively. $\chi = 4\pi/S \, \langle \sum_k \delta(r_k) S_{kz} \rangle_{S_z = S}$ characterizes the density of unpaired electron spins at the nucleus. The dipolar coupling tensor $\boldsymbol{T}$ considers the contribution of dipolar interaction $H_{DD} = \frac{1}{4\pi} \frac{\mu_0}{r^3 h} g_e \mu_B g_N \mu_N \left\{ \boldsymbol{S} \cdot \boldsymbol{I} - \frac{3}{r^2} (\boldsymbol{S} \cdot \boldsymbol{r})(\boldsymbol{I} \cdot \boldsymbol{r}) \right\}$ and is described here by the parameters T and ρ, which depend on the orbitals and ligands involved (*27*), and lead to anisotropic hyperfine coupling $A_x \neq A_y \neq A_z$. Their form is discussed in detail for each atom species below.

The electric quadrupole contribution can be written as

$$\boldsymbol{P} = \begin{pmatrix} P_x & 0 & 0 \\ 0 & P_y & 0 \\ 0 & 0 & P_z \end{pmatrix} = \frac{e^2Qq}{2I(2I-1)h} \begin{pmatrix} -\frac{1}{2}(1-\eta) & 0 & 0 \\ 0 & -\frac{1}{2}(1+\eta) & 0 \\ 0 & 0 & 1 \end{pmatrix} \quad \text{(S4)}$$

where $P_{x,y,z}$ are the components of the electric quadrupole tensor along the principle axis, q is the electric field gradient and Q the nuclear electric quadrupole moment (*27*). This interaction can be viewed as the nuclear counterpart to zero-field splitting of the electron spin $[D_z S_z^2 + E\left(S_x^2 - S_y^2\right)]$. The influence of the electric quadrupole interaction not only shifts the hyperfine energy levels $\propto I_z^2$, it also changes the intensities of the energy transitions reflected in the peak amplitude.

In the framework of this study the external magnetic field was adjusted to $\boldsymbol{B} = |\boldsymbol{B}| \cdot [\cos(\alpha) \cdot \sin(\theta),\ \sin(\alpha) \cdot \sin(\theta),\ \cos(\theta)]$ with $\alpha = 48°$ and $\theta \approx 81°$ with respect to the crystal lattice (See sketches in Fig. 1A and 2A in the main text). In this way the resonance frequencies of both Fe and the two Ti-species lie around 20 GHz.

Section 1.2: Fitting the hyperfine structure: Fits for Ti_O

The separation of the peaks for Ti_O is close to the resolution limit of our setup (*17*). To resolve the hyperfine spectrum including the influence of the quadrupole interaction, measurements were conducted at our lowest possible temperature (0.6 K), at very low current and intermediate RF-voltage. These parameters were found to yield a still detectable signal while the linewidth was small enough to resolve the features caused by nuclear electric quadrupole interaction in the spectrum. Details on the optimization of ESR linewidth and signal can be found in Ref. (*21*). The ESR spectra of both $^{47}Ti_O$ and $^{49}Ti_O$ along with respective spectra for a species of nuclear spin $I = 0$ (e.g. $^{48}Ti_O$) are shown in Fig. S3. The fits are the same as shown in Fig. 3C in the main text.

To explain the observed anisotropic hyperfine ESR spectrum we simulated the data using the EasySpin toolbox (*25*) in Matlab. We assumed a spin of 1/2 and an isotropic g-factor $g_{x,y,z} \approx g$ as in previous works (*19*). Due to the four-fold symmetry of the binding site, we set $\rho = 0$ and $\eta = 0$ in Eq. (S2) and (S4) leading to $A_x = A_y = A_{x,y}$ and $P_x = P_y = P_{x,y} = e^2Qq/4I(2I-1)h$. This results in 4 fit parameters g, $A_{x,y}$, A_z and e^2Qq/h. However, g only accounts for the absolute position of the ESR and does not change the hyperfine spectra notably. The results of this fit are shown in Table S1.

Section 1.3: Fitting the hyperfine structure: Fits for Ti_B

As discussed in the main text, we observe for Ti_B different hyperfine splittings Δf depending on which of the two inequivalent binding site orientations the atom is located. Here, the external magnetic field direction in combination with different values of the g-value and the hyperfine constant in x- and y-direction, $g_x \neq g_y$ and $A_x \neq A_y$, is breaking the symmetry of the two sites. To demonstrate that the different binding site orientations reveal different hyperfine splittings, we used atom manipulation as shown in Fig. S4. The central atom ($^{47}Ti_B$) in the topography in Fig. S4A is moved to in total 8 different binding sites (Fig. S4B). Note that this is the same atom as shown in Fig. 3A in the main text. In Fig. S4C we show the respective ESR spectra that reveal two different configurations. Already the absolute resonance frequencies differ by $\Delta f_0 \approx 200$ MHz [$f_0^h = (22.837 \pm 0.002)$ GHz; vertical: $f_0^v = (22.640 \pm$

0.002) GHz]. By investigating the hyperfine spectra for the two configurations, horizontal and vertical, we find that the hyperfine splitting, Δf, also changes [Fig. S4D, horizontal: $\Delta f^h = (44.9 \pm 0.5)$ MHz; vertical: $\Delta f^v = (48.1 \pm 03)$ MHz].

To explain the observed difference we use the Spin Hamiltonian in Eq. (S1) with anisotropic values for $\mathrm{diag}(\hat{\boldsymbol{g}}) = (g_x, g_y, g_z)$ and $\mathrm{diag}(\hat{\boldsymbol{A}}) = (A_x, A_y, A_z)$ and neglect the electric quadrupole term $P_{x,y,z} = 0$, since no evidence of a significant contribution was found here.

Due to the large angle $\theta = 81°$, we assume a small contribution of the out of plane component $\sin^2(\theta) \approx 1$ and $\cos^2(\theta) \approx 0$ which allows us to ignore the out-of-plane components g_z and A_z. Considering only the remaining in-plane contributions yields (*24*)

$$g = \sqrt{[\cos(\alpha) \cdot g_x]^2 + [\sin(\alpha) \cdot g_y]^2}; \quad A = \frac{1}{g}\sqrt{[\cos(\alpha) \cdot g_x A_x]^2 + [\sin(\alpha) \cdot g_y A_y]^2} \tag{S5}$$

for the effective g-value and the hyperfine constant, respectively. Using symmetry arguments, we can write

$$\begin{aligned} g_x^v = g_y^h = g_x \text{ and } g_y^v = g_x^h = g_y \\ A_x^v = A_y^h = A_x \text{ and } A_y^v = A_x^h = A_y \end{aligned} \tag{S6}$$

where the indices mark a horizontal (h) or a vertical (v) lattice site (Fig. S4B). This already shows that the two different lattice sites can only have a different resonance frequency, if $\alpha \neq 45°$. In previous experiments we found $\alpha \approx 48°$ (*19*). Using Eq. (S5) and (S6) and solving for $g_{x/y}$ and $A_{x/y}$, we obtain

$$g_{x/y} = \sqrt{\frac{1}{2}\left[g_v^2 + g_h^2 \,+/-\, \frac{g_v^2 - g_h^2}{\cos(2\alpha)}\right]}; \quad g_i = \frac{h f_0^i}{\mu_B B} (i = v, h) \tag{S7}$$

$$A_{x/y} = \sqrt{\frac{1}{2g_{x/y}^2}\left[g_v^2 A_v^2 + g_h^2 A_h^2 \,+/-\, \frac{g_v^2 A_v^2 - g_h^2 A_v^2}{\cos(2\alpha)}\right]}; \; A_i = \Delta f^i \;\; (i = v, h) \tag{S8}$$

Using the measured values for Δf and f_0, we can solve Eqs. (S7) and (S8) and obtain the values shown in Table S1. In Fig. S4D we show simulations of the hyperfine spectrum using EasySpin (*25*) with the values in Table S1. We find good agreement with the experimental data. However, the values depend on the exact value of the magnetic field direction α; this is the largest uncertainty here.

Section 1.4: Fitting the hyperfine structure: Fits for Fe

The electronic structure of Fe on MgO is treated in detail elsewhere (*23*). Due to the strong spin-orbit coupling only g_z is contributing in the Zeeman splitting and we can assume $g_{x,y} = 0$. Consequently, only the component $A_z = A$ contributes to the hyperfine splitting and is shown in Table S1 along with the previously determined value for $g_z = g$ (*23*). Since ^{57}Fe is $I = 1/2$, there is no nuclear electric quadrupole interaction.

Section 1.5: Fitting the hyperfine structure: Summary of the results

Table S1 shows the hyperfine parameters for all atomic species and binding sites investigated in this study. The scalar hyperfine constant A is obtained by

$$A = \frac{1}{g}\sqrt{[\sin(\theta)\cos(\alpha)\cdot g_x A_x]^2 + \left[\sin(\theta)\sin(\alpha)\cdot g_y A_y\right]^2 + [\cos(\theta)\cdot g_z A_z]^2} \quad \text{(S9)}$$

It is also shown in Fig. 3D in the main text as Δf. Concerning the g-factors, ESR gives a much higher accuracy than shown in Table S1. Here, we restrict the number of digits due to the uncertainties given by neglecting spin-orbit coupling, by assuming an isotropic g-tensor and by fixing the magnetic field angle.

Section 2: Connecting the hyperfine parameters to the electronic structure

This section discusses the results for the hyperfine constant obtained in the main text and in the previous section. This allows us to obtain further information about the electronic ground state and compare it to theory. Using further theoretical considerations and analyzing the results for different components of A we will determine its different contributions

$$A_i = A_{\mathrm{S}} + A_{\mathrm{D},i} \qquad i = x, y, z \quad \text{(S10)}$$

where A_{S} and $A_{\mathrm{D},i}$ are the Fermi contact and the magnetic dipolar contribution, respectively. As discussed in Eq. (S3), the dipolar contribution has different values for the principal axes making it anisotropic.

Section 2.1: Connecting the hyperfine parameters to the electronic structure: $\mathrm{Ti_O}$

The obtained values for $A_x = A_y$, A_z and e^2Qq/h summarized in Table S1 can be linked to the electronic structure of the Ti-atom. The difference between $A_x = A_y$ and A_z is evidence for additional (anisotropic) dipolar contribution. The hyperfine splitting for a single electron spin in a d_{xy} orbital, neglecting the effects of spin-orbit-coupling, can be expressed by [p. 380 in Ref. (*27*)]

$$\begin{aligned} A_z &= A_{\mathrm{S}} - 4/7\,K \\ A_x = A_y &= A_{\mathrm{S}} + 2/7\,K \end{aligned} \quad \text{(S11)}$$

where $K = g_N g_e(\mu_N/I)\mu_e\langle r^{-3}\rangle$ contains the prefactors as well as the radial part of the dipolar contribution. Since $g_N < 0$ for Ti and χ is usually negative for transition metal atoms in compounds [p. 697 in Ref. (*24*) and Ref. (*30*)], the Fermi-contact term A_{S} defined in Eq. (S3) yields here in total a positive contribution. Similarly $K < 0$ leading to $A_{\mathrm{D}} > 0$ and therefore $A_z > 0$ (we obtain also for $A_x = A_y > 0$ better agreement with the data). This leads to $A_z > A_x = A_y$ as observed in Table S1. In contrast, any other orbital (except $d_{x2\text{-}y2}$) would produce a different dipolar contribution. Therefore, from the difference in the components of A and symmetry arguments we can derive the ground state in agreement with DFT calculations (See methods section).

We obtain $A_{\mathrm{S}}^{47} = +19$ MHz, $\chi^{47} = -1.1$ a. u. and $K^{47} = -34$ MHz leading to $\langle r^{-3}\rangle_{47} = 1.28$ a. u. ($A_{\mathrm{S}}^{49} = +18$ MHz, $\chi^{49} = -1.0$ a. u. and $K^{49} = -32$ MHz leading to $\langle r^{-3}\rangle_{49} = 1.21$ a. u.). Usually $\chi\left(\mathrm{Ti}^{3+}\right) \approx -(2 - 2.5)$ a.u. is found in experiments using transition metal

compounds (30) and $\langle r^{-3} \rangle = 2.55$ a. u. for the free ion from unrestricted Hartree-Fock calculations [p. 399 in Ref. (*24*)]. Since covalency is known to reduce the effect of core polarization [p. 413 in Ref. (*24*) and Ref. (*30*)], the low value of χ suggests a strong bonding with the underlying oxygen atom. The same effect holds for $\langle r^{-3} \rangle$ [p. 414 in Ref. (*24*)].

For the quadrupole contribution we determine $^{49}Q/^{47}Q \approx 0.79$ in excellent agreement with literature [$^{49}Q/^{47}Q = (0.247\text{ b})/(0.3\text{ b}) = 0.82$ (*26*)]. Moreover, using Q from literature we can calculate the electric field gradient to be $q = -0.85$ a. u. from the value of e^2Qq/h in Table S1. Here, the results for q for both isotopes are found to be in good agreement.

Moreover, the electric field gradient of a d_{xy} orbital is given by [p. 357 in Ref. (*27*)]

$$q = -4/7 \cdot \langle r^{-3} \rangle \tag{S12}$$

So that we can determine $\langle r^{-3} \rangle = 1.48$ a. u.. This is in reasonable agreement with the results obtained from the hyperfine constant above and the deviation is most likely caused by neglecting the shielding effects of the electric field [p. 707 in Ref. (*24*)].

The agreement for the values for both isotopes, which represent essentially independent measurements, the correct ratio of quadrupole moments as well as the agreement for $\langle r^{-3} \rangle$ obtained from the dipolar and from electric quadrupole contribution demonstrate the remarkable quality of the fits.

From Eq. (S11) the reason for the reduced hyperfine splitting of Ti_O compared to Ti_B becomes apparent. Since the B-field is pointing mostly in-plane, the $A_{x,y}$-component contributes more than A_z. However, for A_x/ A_y Fermi contact and dipolar contribution oppose each other for Ti_O leading to the reduction. In contrast the out-of-plane component A_z is rather large.

Section 2.2: Connecting the hyperfine parameters to the electronic structure: Ti_B

From the computed magnetization profile obtained from DFT calculations (Fig. 3C) we infer a d_{x^2}-orbital (a d_{z^2}-orbital rotated into the x-direction) to be the ground state for the vertical bridge alignment (horizontal alignment is analogous using a d_{y^2}-orbital). The hyperfine splitting for this configuration can similarly to the Ti_O case be expressed by [p. 380 in Ref. (*27*)]

$$\begin{aligned} A_x &= A_S + 4/7\,K \\ A_y = A_z &= A_S - 2/7\,K \end{aligned} \tag{S13}$$

Here, we neglected the spin-orbit contribution of the d_{z^2}-orbital, which also leads to $g_z \approx g_y$ (*27*).

We obtain $A_S = +50$ MHz, $\chi = -2.8$ a. u. and $K = -37$ MHz leading to $\langle r^{-3} \rangle = 1.35$ a. u. for both isotopes.

The value for the Fermi contact part χ is in contrast to the result for Ti_O close to the value of a free ion. This contributes to the larger hyperfine splitting than for Ti_O. Additionally, the dipolar contribution is only reducing A_x while A_y increases. The latter therefore makes up for the larger hyperfine splitting compared to Ti_O, since for Ti_O both in-plane components are reduced by dipolar coupling.

Section 2.3: Connecting the hyperfine parameters to the electronic structure: Fe

For Fe only the z-component $A_z = 58$ MHz can be determined. This makes it difficult to find the correct contributions of Fermi contact and dipolar contribution. Moreover, spin-orbit interaction might contribute (*27*), due to the high anisotropy of the Fe electron spin on MgO (*23*).

Using literature values ($\chi = -3$ a. u. (*30*) and $\langle r^{-3} \rangle = 5.081$ a. u. [p. 399 in Ref. (*24*)]) we can estimate

$$A_S = 45 \text{ MHz} \qquad K = 114 \text{ MHz}$$

Moreover, approximating the spin-density of Fe on MgO (*23*) as a d_{z2}-orbital, leads to (*27*)

$$A_z \approx A_S + 4/7\, K = 20\text{MHz}$$

Clearly, this value is much lower than observed in the experiment. Since the sign of A_z remains unknown here, we suggest two possible scenarios.

First, for the free ion case a hyperfine constant of $A = A_z = +38$ MHz was found from atomic beam experiments (*31*). Here, the Fermi-contact contribution is much lower ($A_S = 5$ MHz) than the dipolar contribution ($4/7\, K = 43$ MHz) and opposite in sign. This result is already significantly closer to our experimental result and additional consideration of contributions from spin-orbit-coupling might increase *A* further.

Second, in some crystals Fe shows an increased Fermi contact part, e.g. sodium fluoride ($A_S = 74$ MHz, $A_z = 141$ MHz) (*32*). In contrast the dipolar contribution is lowered ($\sim$20 MHz). This would lead to a value close to the one found here with a negative sign for A_z.

Both A_S and K depend on the binding configuration of Fe on MgO. Therefore, it is likely that both deviate from the two extreme cases pointed out above. However, at least one contribution needs to be sufficiently large to explain the experimentally observed value. In Fig. 1C in the main text the case of positive A_z is shown, for which the nuclear spin and electron spin are anti-aligned.

Section 2.4: Connecting the hyperfine parameters to the electronic structure: Relative nuclear magnetic moment of Ti

Since both the dipolar contribution *P* as well as the Fermi-contact part A_S are proportional to μ_N/I, we can obtain the relative ratio of the nuclear magnetic moments by

$$\frac{A^{47}}{A^{49}} = \frac{g_N^{47}/\frac{5}{2}}{g_N^{49}/\frac{7}{2}}, \tag{S14}$$

which is equal to 1.000 when using the literature values $g_N^{47} = -0.7884$ and $g_N^{49} = -1.1040$ (*24*). For Ti_B we find for both isotopes $A^{47}/A^{49} = 0.99$ showing no significant deviation from 1 as expected. For Ti_O we obtain $A^{47}/A^{49} \approx 1.07$, as a consequence of the smaller splitting and the additional contribution of quadrupole interaction. Since we only obtain the relative ratio of the nuclear magnetic moments, literature values were used for extracting χ and $\langle r^{-3} \rangle$ in the discussion above.

Section 3: Hyperfine model for Ti dimers

Here, we model the spin system formed by the two $S = 1/2$ electronic spins of a Ti dimer. One of them, labeled as S_1, has a nuclear spin. The solution for an exchange-coupled dimer is given in greater detail in Ref. (*19*,*20*). It is here extended by the hyperfine coupling AI_zS_{1z} as a perturbation term leading to

$$H \cong \gamma_1 \hbar S_{1z}(B_{\text{ext}} + B_{\text{tip}}) + AI_zS_{1z} + \gamma_2 \hbar S_{2z} B_{\text{ext}} + JS_{1z}S_{2z} + \frac{J}{2}(S_1^+S_2^- + S_1^-S_2^+) \tag{S15}$$

where the indices 1, 2 indicate the $^{47}\mathrm{Ti_B}$ ($I = 5/2$) and $^{48}\mathrm{Ti_O}$ atom ($I = 0$) in Fig. 4A in the main text, respectively. Note that here, in contrast to the rest of this work, we define the *z* direction as the direction of the external magnetic field B_{ext}. In addition, B_{tip} is the local field of the tip acting in good approximation on $^{47}\mathrm{Ti_B}$ only. $\gamma_{1,2}$ are the gyromagnetic ratios and J is the exchange coupling constant.

We first provide a simple perturbation theory argument to show that the hyperfine correction to the energy levels of the system is proportional to the average magnetization of the spin S_{1z}. For that matter, we considered the unperturbed wave functions as the tensor products of the electronic wave functions Φ_e and the nuclear spin wave function, labeled with the eigenstate of the nuclear spin operator m_I. The shift of the unperturbed energy levels due to the hyperfine interaction AI_zS_{1z} is given by

$$E_e(m_I) = A\langle \Phi_e, m_I | S_{1z} I_z | \Phi_e, m_I \rangle = A m_I \langle \Phi_e | S_{1z} | \Phi_e \rangle \tag{S16}$$

As a result, the correction to the transition energy between states e and e' is given by:

$$\delta E_{ee'} = E_e - E_{e'} = A m_I (\langle \Phi_e | S_{1z} | \Phi_e \rangle - \langle \Phi_{e'} | S_{1z} | \Phi_{e'} \rangle) \tag{S17}$$

These equations make it clear that the hyperfine correction is sensitive to the average magnetization of the electronic spin of atom 1. With this equation we can right away get a first estimate for the cases:

In the case where the states e and e' describe eigenstates of S_{1z} with opposite spin, Eq. (S19) give a hyperfine correction of $\delta E_{ee'} = A m_I$. Here, the electronic spin of the first atom is completely uncorrelated from the second.

In the case of a singlet-triplet transition as shown in Fig. 4B in the main text, the average magnetization of both the initial and final state is unchanged $\langle \Phi_{\mathrm{S0}} | S_{1z} | \Phi_{\mathrm{S0}} \rangle = \langle \Phi_{\mathrm{T0}} | S_{1z} | \Phi_{\mathrm{T0}} \rangle$, resulting in no hyperfine correction $\delta E_{\mathrm{S0,T0}} = 0$.

If one of the involved states is either $\mathrm{S_0}$ or $\mathrm{T_0}$, the splitting is cut in half, e.g. $\delta E_{\mathrm{T-,T0}} = A/2\, m_I$.

In the following we discuss the full solution of Eq. (S15). Solving the Hamiltonian leads to the wavefunctions

$$\begin{aligned} |\mathrm{T_+}\rangle &= |{\downarrow\downarrow}\rangle \\ |\mathrm{T_0}\rangle &= \sin\frac{\xi}{2}|{\uparrow\downarrow}\rangle + \cos\frac{\xi}{2}|{\downarrow\uparrow}\rangle \\ |\mathrm{T_-}\rangle &= |{\uparrow\uparrow}\rangle \\ |\mathrm{S_0}\rangle &= \cos\frac{\xi}{2}|{\uparrow\downarrow}\rangle - \sin\frac{\xi}{2}|{\downarrow\uparrow}\rangle \end{aligned} \tag{S18}$$

$$\tan\xi = \frac{J}{\gamma_1\hbar\left(B_{\mathrm{ext}} + B_{\mathrm{tip}}\right) - \gamma_2\hbar B_{\mathrm{ext}} + A m_I} = \frac{J}{h\Delta f_0 + A m_I}$$

where $|\mathrm{T_+}\rangle$, $|\mathrm{T_0}\rangle$ and $|\mathrm{T_-}\rangle$ are triplet and $|\mathrm{S_0}\rangle$ a singlet state. $h\Delta f_0 = \gamma_1\hbar\left(B_{\mathrm{ext}} + B_{\mathrm{tip}}\right) - \gamma_2\hbar B_{\mathrm{ext}} = h(f_0^{\mathrm{TiB}} - f_0^{\mathrm{TiO}})$ is the effective detuning due to the presence of the tip field as well as unequal gyromagnetic ratios of both atoms. The arrows indicate the alignment of the two

electron spins and the influence of the nuclear spin is considered in the term Am_I. The respective eigenvalues are

$$\begin{aligned} E_{\mathrm{T}+} &= \frac{J}{4} + \frac{1}{2}\left(\gamma_1\hbar(B_{\mathrm{ext}} + B_{\mathrm{tip}}) + \gamma_2\hbar B_{\mathrm{ext}} + Am_I\right) \\ E_{\mathrm{T}0} &= -\frac{J}{4} + \frac{1}{2}\sqrt{J^2 + (h\Delta f_0 + Am_I)^2} \\ E_{\mathrm{T}-} &= \frac{J}{4} - \frac{1}{2}\left(\gamma_1\hbar\left(B_{\mathrm{ext}} + B_{\mathrm{tip}}\right) + \gamma_2\hbar B_{\mathrm{ext}} + Am_I\right) \\ E_{\mathrm{S}0} &= -\frac{J}{4} - \frac{1}{2}\sqrt{J^2 + (h\Delta f_0 + Am_I)^2} \end{aligned} \tag{S19}$$

These energies correspond to those shown in Fig. 4B in the main text. As can be seen, $E_{\mathrm{T}0}$ and $E_{\mathrm{S}0}$ are independent of B_{ext} as long as $J \gg h\Delta f_0 + Am_I$. One of the transitions shown in the main text in Fig. 4C is then given by

$$\begin{aligned} hf_{\mathrm{T}-,\mathrm{T}0} &= E_{\mathrm{T}0} - E_{\mathrm{T}-} \\ &= -\frac{J}{2} + \frac{1}{2}\left(\gamma_1\hbar\left(B_{\mathrm{ext}} + B_{\mathrm{tip}}\right) + \gamma_2\hbar B_{\mathrm{ext}} + Am_I\right) + \frac{1}{2}\sqrt{J^2 + (h\Delta f_0 + Am_I)^2} \end{aligned} \tag{S20}$$

Consequently $\Delta f_{\mathrm{T}-,\mathrm{T}0}$ for $\Delta m_I = 1$ transitions, for instance $m_I = \pm 1/2$, is given by

$$\begin{aligned} h\Delta f_{\mathrm{T}-,\mathrm{T}0} &= \frac{A}{2} + \frac{1}{2}J\left[\sqrt{1 + ([h\Delta f_0 + A/2]/J)^2} - \sqrt{1 + ([h\Delta f_0 - A/2]/J)^2}\right] \\ &\approx \frac{A}{2}\cdot\left[1 + \frac{h\Delta f_0}{J}\right] \end{aligned} \tag{S21}$$

Here, we made a Taylor expansion in the last approximation. Fully mixed-states ($\Delta f_0 = 0$) would therefore be obtained for $A/2h = 22.5$ MHz. The state mixing, defined here as $\frac{2\xi}{\pi} = \mathrm{atan}\left[\left(\frac{2h\Delta f_{\mathrm{T}-,\mathrm{T}0}}{A} - 1\right)^{-1}\right]/\frac{\pi}{2}$, can thus be deduced to be 87% using the experimental hyperfine splitting of $\Delta f_{\mathrm{T}-,\mathrm{T}0} = 27.2$ MHz.

In contrast, for the singlet-triplet transition, also shown in Fig 4C, we find

$$hf_{\mathrm{S}0,\mathrm{T}0} = E_{\mathrm{T}0} - E_{\mathrm{S}0} = J\sqrt{1 + ([h\Delta f_0 + Am_I]/J)^2} \approx J\cdot\left[1 + \frac{1}{2}([h\Delta f_0 + Am_I]/J)^2\right] \tag{S22}$$

Consequently, $\Delta f_{\mathrm{S}0,\mathrm{T}0}$ for $\Delta m_I = 1$ transitions is given by

$$\Delta f_{\mathrm{S}0,\mathrm{T}0} \approx \frac{A\Delta f_0}{J} \approx 2h\Delta f_{\mathrm{T}-,\mathrm{T}0} - A \tag{S23}$$

where in the last step we made use of Eq. (S21). Using $\Delta f_{\mathrm{T}-,\mathrm{T}0} = 27.2$ MHz and $A = 44.9$ MHz we obtain $\Delta f_{\mathrm{S}0,\mathrm{T}0} \approx 9$ MHz. For the transition of $f_{\mathrm{S}0,\mathrm{T}0}$ no hyperfine splitting is visible in agreement with the predicted reduction in Eq. (S23). Though a hyperfine splitting of 9 MHz is

within the energy resolution of our setup, the additional reduction in peak intensity of the singlet-triplet transition makes resolving the remaining splitting difficult, so that in this case it only contributes to the general broadening of the peak. Taking additionally the absolute peak position for the singlet-triplet transition ($f_{\mathrm{S0,T0}} = 29.72$ GHz) into account, we can determine the exchange coupling constant using Eq. (S21) and (S22) to be $J/h = (29.1 \pm 0.2)$ GHz.

References and Notes:

33. B. E. Kane, *Nature* **393**, 133–137 (1998).
34. B. B. Blinov, D. Leibfried, C. Monroe, D. J. Wineland, *Quantum Information Processing* **3**, 45–59 (2004).
35. S. Thiele *et al.*, *Science* **344**, 1135–1138 (2014).
36. J. Köhler, A. C. J. Brouwer, E. J. J. Groenen, J. Schmidt, *Science* **268**, 1457–1460 (1995).
37. R. Vincent, S. Klyatskaya, M. Ruben, W. Wernsdorfer, F. Balestro, *Nature* **488**, 357–360, (2012).
38. P. Neumann *et al.*, *Science* **329**, 542–544 (2010).
39. J. J. Pla et al., *Nature* **496**, 334–338 (2013).
40. Y. Sugimoto *et al.*, *Nature* **446**, 64–67 (2007).
41. L. Gross, F. Mohn, N. Moll, P. Liljeroth, G. Meyer, *Science* **325**, 1110–1114 (2009).
42. A. J. Heinrich, J. A. Gupta, C. P. Lutz, D. M. Eigler, *Science* **306**, 466–469 (2004).
43. S. Loth, M. Etzkorn, C. P. Lutz, D. M. Eigler, A. J. Heinrich, *Science* **329**, 1628–1630 (2010).
44. A. A. Khajetoorians *et al.*, *Science* **339**, 55–59 (2013).
45. B. C. Stipe, M. A. Rezaei, W. Ho, *Science* **280**, 1732–1735 (1998).
46. F. D. Natterer, F. Patthey, H. Brune, *Phys. Rev. Lett.* **111**, 175303 (2013).
47. F. Delgado, J. Fernández-Rossier, *Phys. Rev. Lett.* **107**, 076804 (2011).
48. C. R. Ast *et al.*, *Nat. Commun.* **7**, 13009 (2016).
49. S. Baumann *et al.*, *Science* **350**, 417–420 (2015).
50. W. Paul, S. Baumann, C. P. Lutz, A. J. Heinrich, *Rev. Sci. Instrum.* **87**, 074703 (2016).
51. K. Yang *et al.*, *Phys. Rev. Lett.* **119**, 227206 (2017).
52. Y. Bae *et al.*, submitted (2018).
53. P. Willke *et al.*, *Sci. Adv.* **4**, eaaq1543 (2018).
54. Materials and methods are available as supplementary materials on Science Online.
55. W. Paul *et al.*, *Nat. Phys.* **13**, 403–407 (2017).
56. A. Abragam, B. Bleaney, Electron paramagnetic resonance of transition ions (OUP Oxford, Reprinted Ed. 2012).

57. S. Stoll, A. Schweiger, *J. Magn. Res.* **178**, 42–55 (2006).

58. K. H. Channappa, J. M. Pendlebury, *Proc. Phys. Soc.* **86**, 1145–1146 (1965).

59. F. E. Mabbs, D. Collison, *Electron paramagnetic resonance of d transition metal compounds* (Vol. 16). Elsevier (2013).

60. T. Choi *et al.*, *Nat. Nanotechnol.* **12**, 420–424 (2017).

61. J. J. van der Klink, H. B. Brom, *Prog. Nucl. Magn. Reson. Spectrosc.* **36**, 89-201 (2000).

62. B. R. McGarvey, *J. Chem. Phys.* **71**, 51–66 (1967).

63. W. J. Childs, L. S. Goodman, *Phys. Rev.* **148**, 74–78 (1966).

64. T. P. P. Hall, W. Hayes, R. W. H. Stevenson, J. Wilkens, *J. Chem. Phys.* **39**, 35–39 (1963).

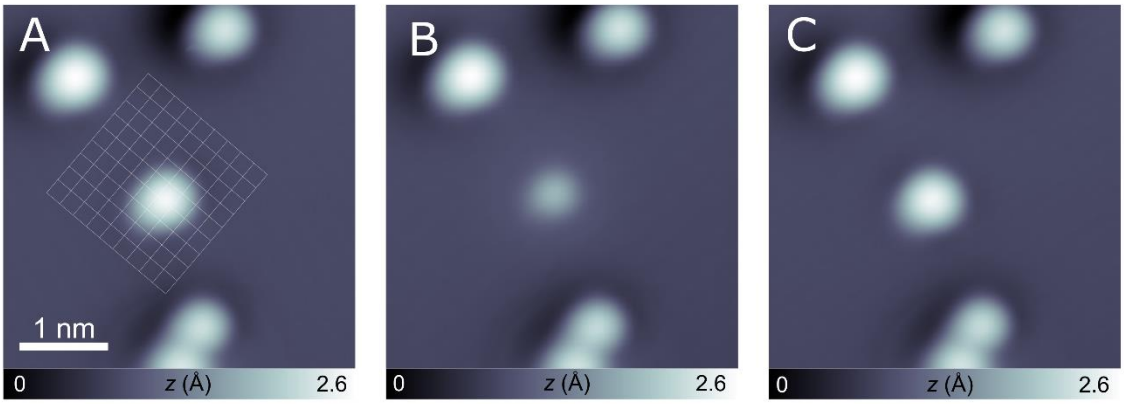

Fig. S1.

Large-scale topographies of the atom in Fig. 3 in the main text showing surrounding adatoms for position reference. Constant-current topography of a Ti atom (center) on **(A)** a horizontal bridge binding site **(B)** an oxygen binding and **(C)** a vertical bridge binding site ($I_{\mathrm{set}} = 10$ pA, $V_{\mathrm{DC}} = 40$ mV for all measurements).

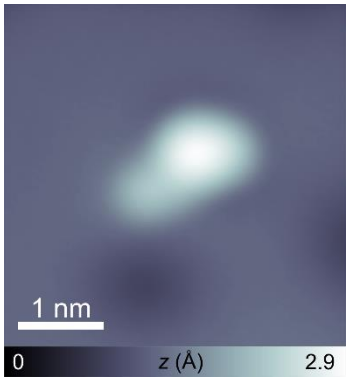

Fig. S2
Large-scale topography of the dimer in Fig. 4 in the main text.

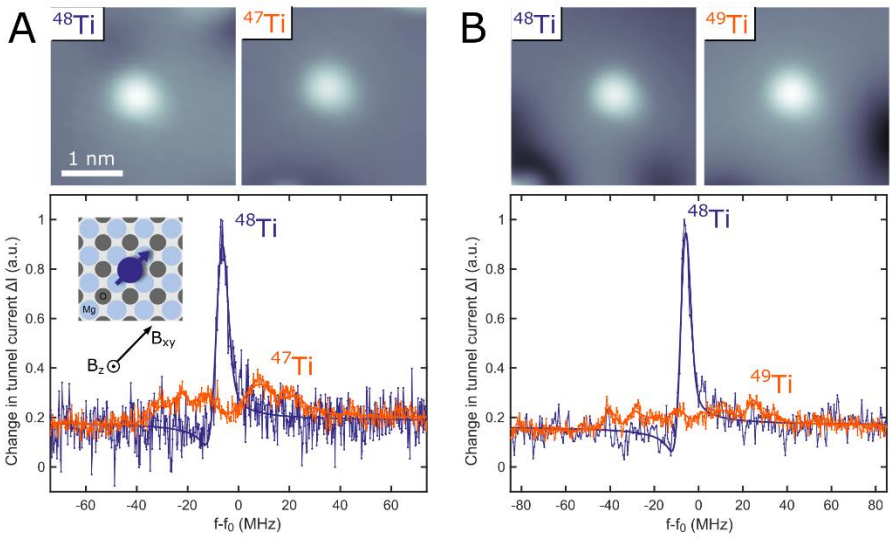

Fig. S3

Hyperfine interaction for titanium on an oxygen binding site (Ti_O). ESR spectra (orange) for **(A)** ^{47}Ti ($I = 5/2$, tunneling parameters: $I_{set} = 1.5$ pA, $V_{DC} = 60$ mV, $V_{RF} = 25$ mV) and **(B)** ^{49}Ti ($I = 7/2$, tunneling parameters: $I_{set} = 1.5$ pA, $V_{DC} = 60$ mV, $V_{RF} = 25$ mV) on an oxygen binding site (See inset in A). Respective reference spectra taken on a nuclear spin free isotope, e.g. ^{48}Ti, are shown in blue (same tunneling parameters). The topographies of the respective atoms are shown on top.

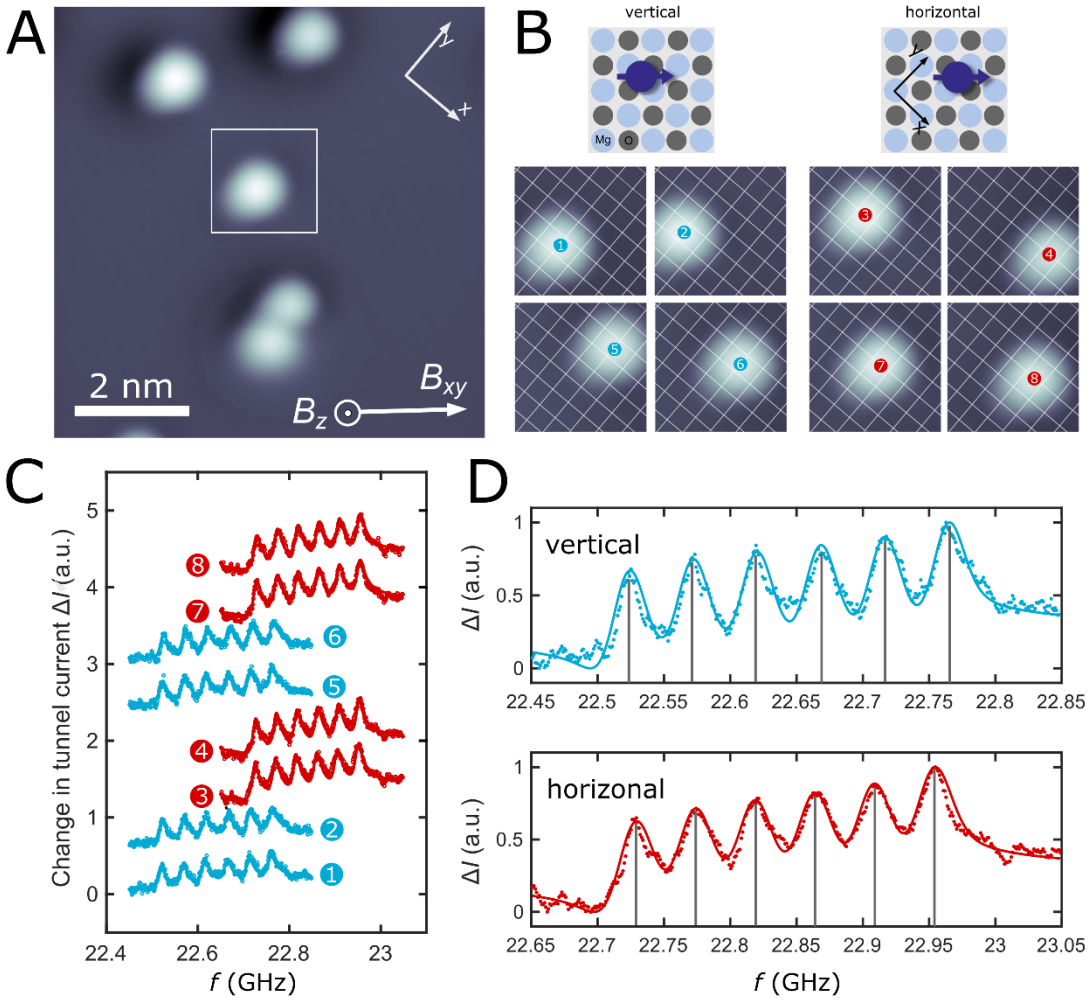

Fig. S4

Binding site analysis for Ti_B. **(A)** STM topography of the area around an isolated $^{47}Ti_B$ atom (I_{set} = 10 pA, V_{DC} = 40 mV). **(B)** Using the STM tip, the atom is moved across the surface to different binding sites. The horizontal (vertical) lattice position is indicated in red (blue). **(C)** ESR spectra taken for the 8 different configurations as shown in (B) (I_{set} = 20 pA, V_{DC} = 40 mV, V_{RF} = 25 mV). **(D)** Averaged spectra of the data in (C) for the two binding sites. The black lines emphasize the change in splitting. Solid lines are fits using the EasySpin toolbox.

Species	S	I	g	$A = (A_x, A_y, A_z)$ [MHz]	e^2Qq/h [MHz]
^{57}Fe	2	1/2	$g_z = 2.6$	$A_z = 58$	0
^{47,49}Ti$_B$ (vertical)	1/2	5/2, 7/2	$g_x = 1.90$ $g_y = 1.75$	$48.1 = (29.1, 61.0, 61.0)$	−
^{47,49}Ti$_B$ (horizontal)	1/2	5/2, 7/2	$g_x = 1.75$ $g_y = 1.90$	$44.9 = (61.0, 29.1, 61.0)$	−
^{47}Ti$_O$	1/2	5/2	1.78	$11.3 = (9.6, 9.6, 39.1)$	−61
^{49}Ti$_O$	1/2	7/2	1.78	$10.7 = (9.1, 9.1, 36.9)$	−48

Table S1.

Hyperfine parameters extracted for the atoms analyzed in this work.